HOLOGRAPHIC 'CAP' COLLECTORS FOR ENHANCED

MID-DAY ENERGY PRODUCTION OF VERTICALLY-MOUNTED BIFACIAL

PHOTOVOLTAIC MODULES

by

Silvana Ayala Peláez

_____

A Report Submitted to the Faculty of the

COLLEGE OF OPTICAL SCIENCES

In Partial Fulfillment of the Requirements

For the Degree of

MASTER OF SCIENCE

In the Graduate College

THE UNIVERSITY OF ARIZONA

2018

STATEMENT BY AUTHOR

–

The report titled *Holographic 'cap' collectors for enhanced mid-day energy production of vertically-mounted bifacial photovoltaic modules* prepared by *Silvana Ayala Peláez* has been submitted in partial fulfillment of requirements for a master's degree at the University of Arizona and is deposited in the University Library to be made available to borrowers under rules of the Library.

Brief quotations from this report are allowable without special permission, provided that an accurate acknowledgement of the source is made. Requests for permission for extended quotation from or reproduction of this manuscript in whole or in part may be granted by the copyright holder.

SIGNED: *Silvana Ayala Peláez*

APPROVAL BY THESIS DIRECTOR

This thesis has been approved on the date shown below:

Raymond K. Kostuk   *Defense date*
Professor of Optical Sciences College and ECE department   *09/06/2018*

ACKNOWLEDGEMENTS

Eternally grateful to my mother, who has shown me every day the value in tenacity, courage, and love. However, this report and masters is dedicated to my father, for this week is his first birthday we will not spend together. I'm an engineer thanks to him.

I would like to express my deepest gratitude to my advisor, Dr. Raymond K. Kostuk. His mentoring has challenged me to grow during the past couple years beyond my imagination. I've approached optical science under his tutelage and discovered its many joys and foibles under his expertise and kindness. This is a path I had not foreseen but that I'm very glad I followed.

I would also like to thank Dr. Koshel and Dr. Milster, not only for being in my committee, but for both being excellent educators that shared with me their passion for their work. I've seen the art of optics through both of your lenses and I'm forever awed by it.

This journey would of course not have been possible without the support of my lab partners, Women in Optics, QESST Scholars, NREL colleagues, family and friends. You are all awesome and I love you all.

Table of Contents

Contents

List of Figures

LIST OF TABLES

7

ABSTRACT

The most expensive electrical energy occurs during early morning and late afternoon time periods [1]. Meeting demand during these times poses a problem for fixed latitude mounted photovoltaic (PV) systems since the sun is low in the sky. One potential solution is to use vertically-mounted bifacial PV modules to increase the East-West collection area and solar energy production during high energy usage time periods. However, vertically-mounted PV modules have reduced conversion efficiency during mid-day time periods. In this paper the use of a horizontally mounted collector with holographic elements is examined as a way of increasing the energy yield of vertically-mounted bifacial PV modules during mid-day time periods. A design of a holographic 'cap' collector that considers dimensional constraints, holographic diffraction efficiency characteristics, and solar collection efficiency properties is evaluated. The irradiance illuminating the module is modeled with and without the cap.

Chapter 1: Bifacial Solar Panels

Bifacial solar panel technology has been around since 1977[2], developed for space applications that benefited from its glass-on-glass encasing that allowed light capture from both sides of a solar cell. In recent years it has gained increased attention due to silicon solar technology improvements. New techniques for implementing Passivated Emitter and Rear Cell Technology (PERC) in manufacturing of solar cells (like PERC+, and nPERC for bifacials), as well as in Heterojunction with Intrinsic Thin-layer (HIT) cell manufacturing have allowed bifacial solar cells to reach comparable efficiencies to those of traditional monofacial silicon solar cells [3]. Bifacials offer the same efficiency with increased overall energy yield through the capture of irradiance on its rear-side (Figure 1).
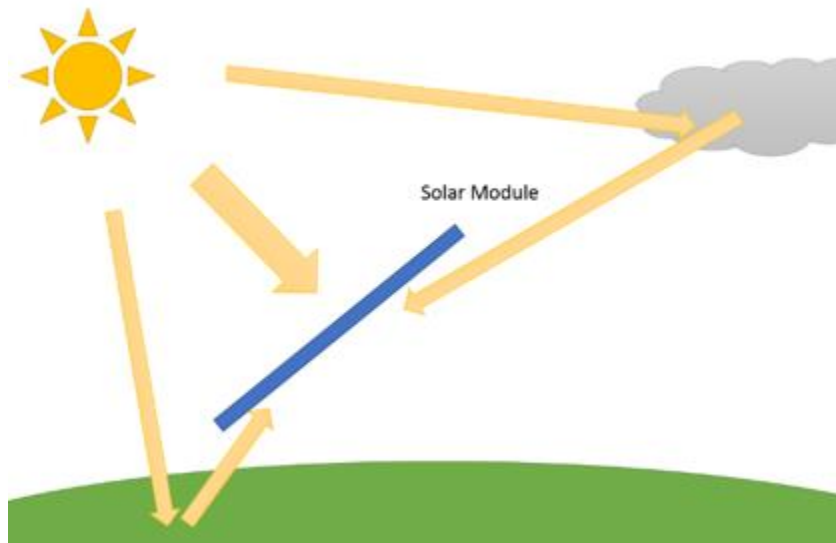
Figure 1 - Bifacial modules convert solar energy into electricity from both sides of the module, taking advantage of diffuse light as well.

An additional benefit of the use of glass-glass module packaging for bifacial modules are reduced temperatures in the cells, which provide greater operational lifetimes than metal-backed modules [4].

Therefore, bifacial modules can produce more energy over the useful operating lifetime and thereby reduce operating cost. However, bifacial modules' potential performance for different deployments is still not very well understood or expressed through any common industry standard [5], [6]. Much research is being done to provide industry and stakeholders with guidelines for best mounting and for more accurate expected performances.

There is also interest in using bifacial modules in the field of Building Integrated Photovoltaics, or in other niche applications like vertically-mounted photovoltaic solar panels. Four of the 5 largest solar cells producers are already evaluating or producing bifacial modules (JinkoSolar, Trina Solar, Canadian Solar, Hanwha Q-Cell and JA Solar) [3],and bifacial market share projections reach 30% by 2027 [7].

1.1 Properties

Under the same standard conditions (1000 W/m^2 at 25 C), the power produced by the front versus the rear side of a bifacial panel will differ, due to semiconductor properties or the amount of back contact metallization. This is quantified with a bifacial factor φ_{Pmp} [8]:

$$\varphi_{Pmp} = \frac{Pmp,rear}{Pmp,front} \times 100\%$$ (1)

There are reports in literature of bifacial factors as high as 99% [9], and commercial panels with a 90% bifacial factor [10]. The additional power produced by bifacial cells/modules over monofacial cells/modules is known as bifacial gain BG, and is used as a metric to evaluate bifacial module performance [11]:

$$BG[\%] = \varphi_{Pmp} \times \frac{P_{bifacial}}{P_{bifacial}}(1 - \eta_{loss})$$ (2)

The η_{loss} term reflects power losses caused by nonuniform rear-side irradance and/or rear shading. The bifaciality gain is an electrical parameter, but for a simple calculation of the output of a panel, it can be considered as an optical parameter as well considering the irradances reaching the front and rear of the panel (G_{front} and G_{rear}), particularly when $\eta_{loss} = 0$ and $\varphi_{Pmp} = 100\%$:

$$BG_E = \frac{G_{rear}}{G_{front}} \tag{3}$$

The electrical model for a bifacial solar cell can be seen in Figure 2. The current produced from the irradiance received in the rear side is modeled as an extra current source, which can be simplified to a single current source with input $G_{rear} + G_{front}$ [12].
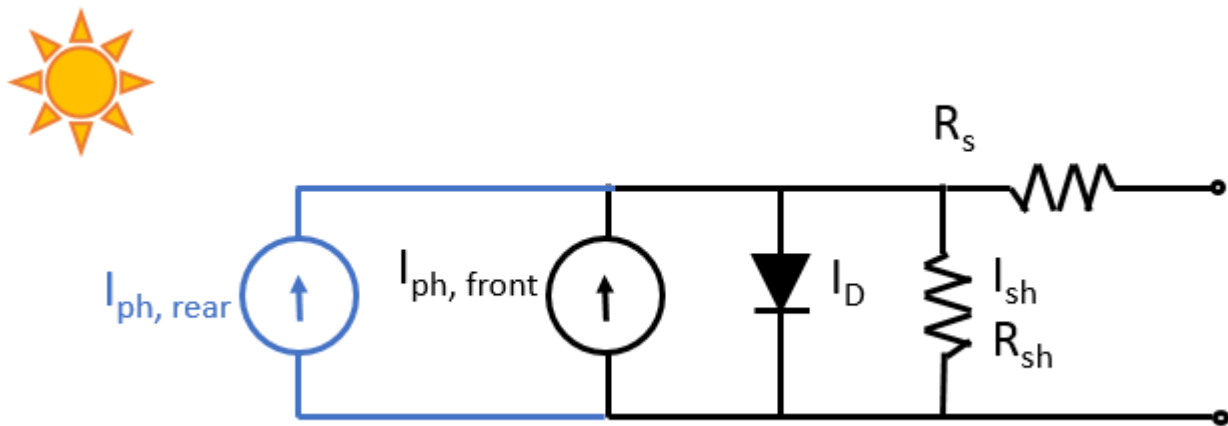
Figure 2 - Electrical model for a bifacial cell. The difference to the electrical model of a monofacial cell is highlighted in blue: the extra current generated from the rear-side is considered as an added current source. Both front and rear sources have the same diode voltage drop.

1.2 Rear Side Irradiance

Rear-surface irradiance modeling is a performance modeling unique to bifacial modules. While front-irradiance is very well understood, rear-side irradiance is a result of both illumination and system parameters. Illumination is dependent on the geographical location's conditions due to sun position,

direct and diffuse radiation components, and climate. System parameters to consider are row-to-row distance, clearance from the ground, tilt, and the albedo of the underlying surface. Techniques for rear-surface irradiance modeling fall into three categories: ray tracing models, which simulate multipath reflection and absorption of individual rays entering a scene [13], [14]; view factor approaches, which assume isotropic scattering of reflected rays and so permit calculation of irradiance by integration [12], [15], [16] and empirical models representing the relationship between measured quantities, e.g. between direct and diffuse irradiance, and measured rear-surface irradiance [10]. A short summary can be seen in Table 1, and a more in-depth comparison is available in [11].

Table 1 - Models for bifacial-irradiance simulation

Model Name	Type of Model	Short Description
Prism Solar Model **[10], [17]**	Empirical	Two different models available, one in Prism solar design guide and one in their IEEE journal. One panel assumed, input parameters panel tilt, ground clearance, and albedo.
Solar World Model **www.solarworld.de/fileadmin/calculator**	Empirical	Calculator for bifacial gain for Solar World panel Bisun Protect 290. Allows for different installation types, mounting heights, row pitches. albedo and panel orientations.
NREL View Factor Model **https://github.com/NREL/bifacial_radiance**	View factor	Freeware. Very fast runtime and low memory requirement. Used for systems with regular row layouts (infinite number assumed)

PVSyst www.psyst.com	View factor	Commercial software package, most used in industry. Assumes infinite number of rows and Lambertian isotropic sky.
NREL Radiance Bifacial Model https://github.com/NREL/bifacial_radiance	Raytrace	Freeware. Complex scenes can be created, and any number of modules per row and rows. Fast run time when using sky preprocessing (cumulative sky). Uses reverse ray tracing.
FRED-Bifacial Raytrace https://github.com/shirubana/FRED-GenCumSky	Raytrace	Developed for this paper. Complex scenes can be created, and any number of modules per row and rows. Uses reverse ray tracing.

Figure 3 shows a comparison of currently available bifacial rear side irradiance models described in [11] and their sensitivity to varying module tilt, module height, row-to-row spacing, and ground albedo for a bifacial solar array. The model developed in this report (explained in following chapters) is also included for comparison and validation. The basic array parameters are 0.15m ground clearance, 1.5 m row to row spacing, tilt of 10 degrees, albedo of 0.62, for the location of Richmond, VA. Typical meteorological year data (TMY3) data for this location was used to calculate the yearly rear-side irradiance gains [18].Geometrical factor models assume infinite number of rows and modules, while raytrace models included in the comparison use 7 rows of 20 modules for their comparison. It has been explored that this assumption is enough to converge into the infinite assumption for raytrace models [11].
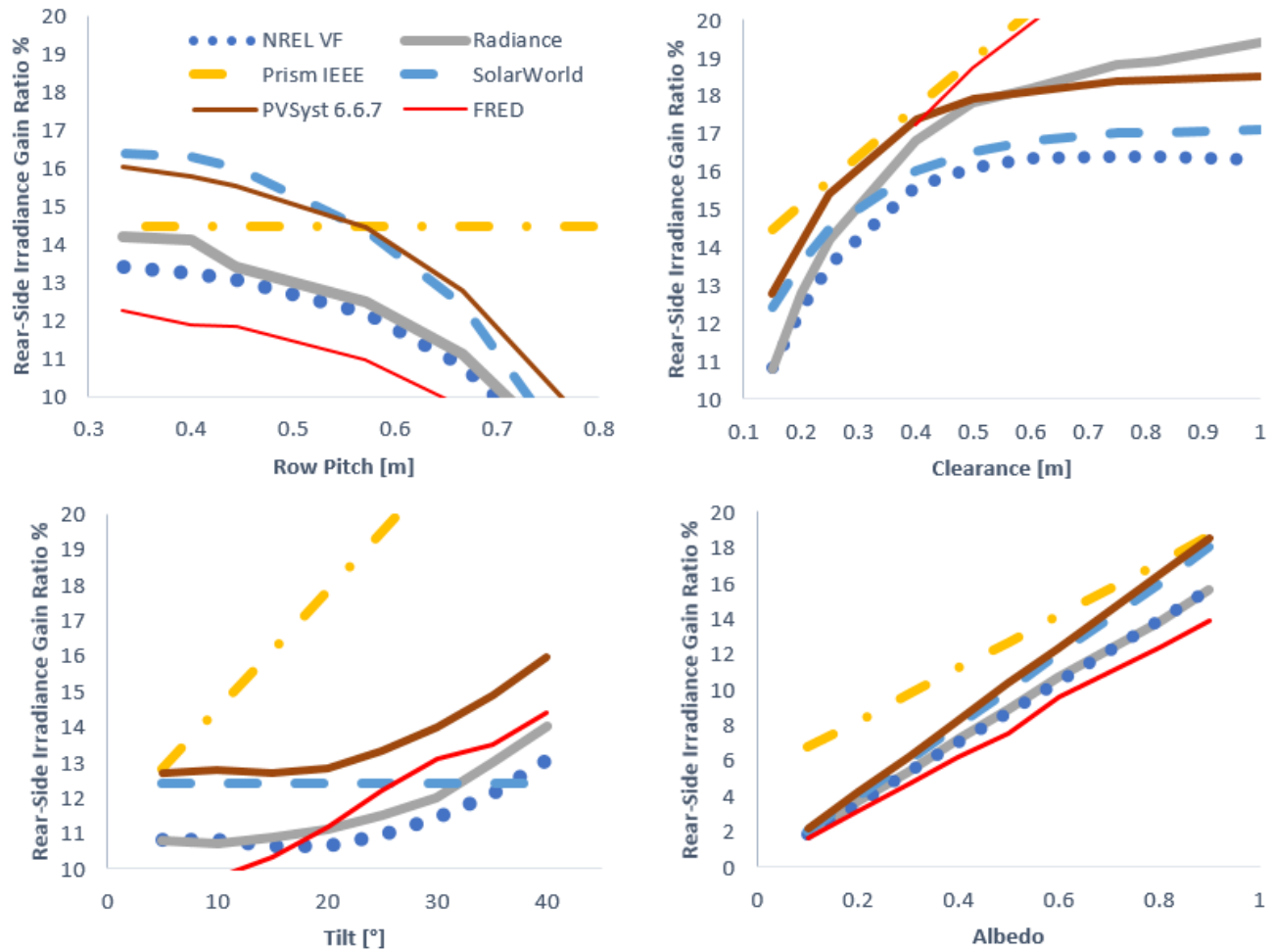
Figure 3 – Rear-surface irradiance gain ratio calculated with different commercially available models.

1.3 Vertically-Mounted Bifacials

Monofacial PV panels collect direct and diffuse light illuminating their front side, and only a small fraction of light reflected from ground and other nearby objects. To maximize the energy production through the whole year for fixed-tilt mounting, panels are usually mounted facing south and with a tilt equal to the latitude angle of the location Figure 4. Bifacial modules collect both direct and diffuse ground reflected light, allowing more flexibility in their mounting and applications. In particular,

vertically-mounted photovoltaics benefit from bifaciality to produce light in the morning and afternoons with an East/West orientation.
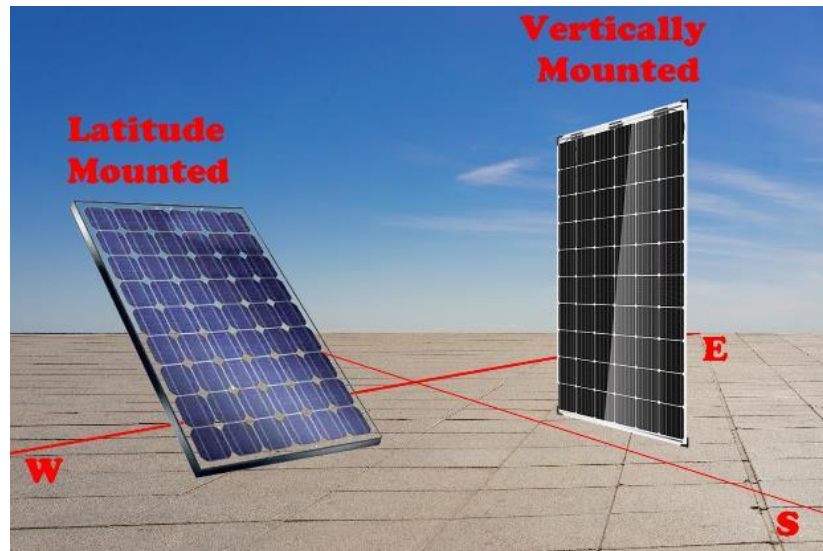
Figure 4 - Latitude mounted module versus vertically-mounted module.

East/West vertically-mounted bifacials generate most of their electricity during early morning and late afternoon when the sun is incident at near normal angles of incidence. This happens to match the times of day with highest electricity demand. Figure 5 shows a typical electric demand shape for a day, in this case for August 14, 2008 for California [19]. The demand peaks in the late afternoon, which is a common trend seen by utility companies. The demand minus the production by solar and wind is also plotted, and is known as the duck chart or duck curve [20]. It is a challenge for utilities to provide the most low-cost energy possible for the peaks around this duck-curve, and a combination of other sources of energy must be used.

Electric Demand for California

demand

demand minus solar and wind
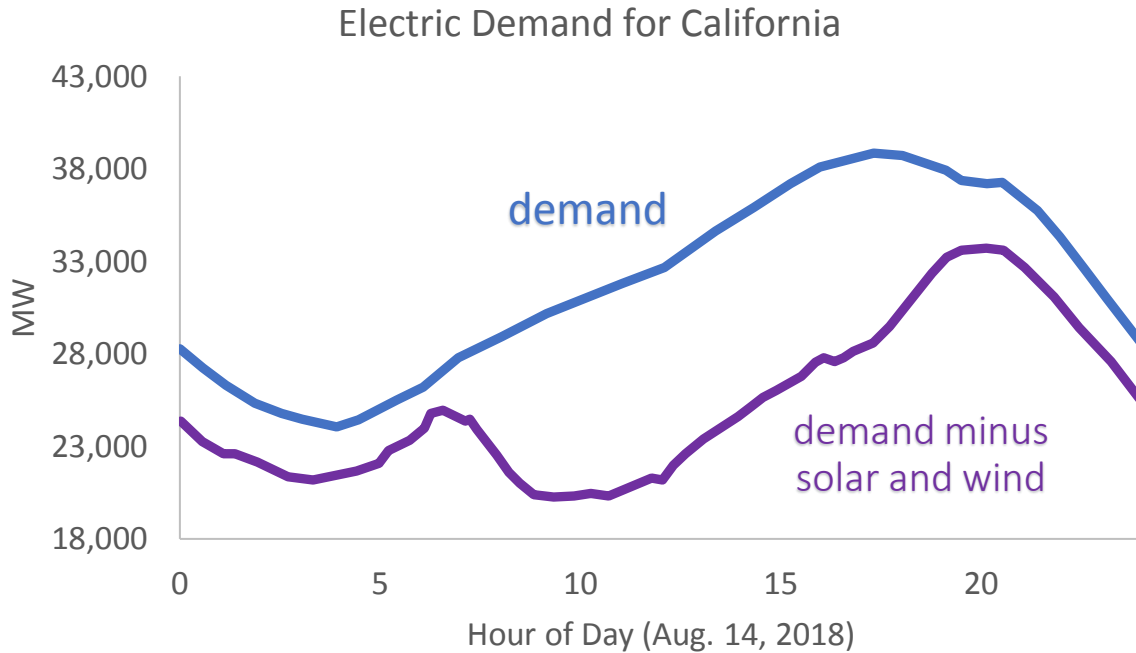
Figure 5 - Electric demand for California for the day of August 14, 2018. Data available to public on http://oasis.caiso.com.

Figure 6 shows the measured power distribution for a mono-facial panel mounted at latitude in Tucson, AZ, and a bifacial mounted East/West for one day. On the right of the figure, the same day has been modeled using the View Factor Model developed by the National Renewable Energy Laboratory [15], [21]. As can be seen, a double-hump is present in the irradiance/production reaching the vertical-mounted bifacial solar module, which are sensitive to variations in azimuth angle [22], and at this particular times the incident angles on the panel are the lowest for the day.
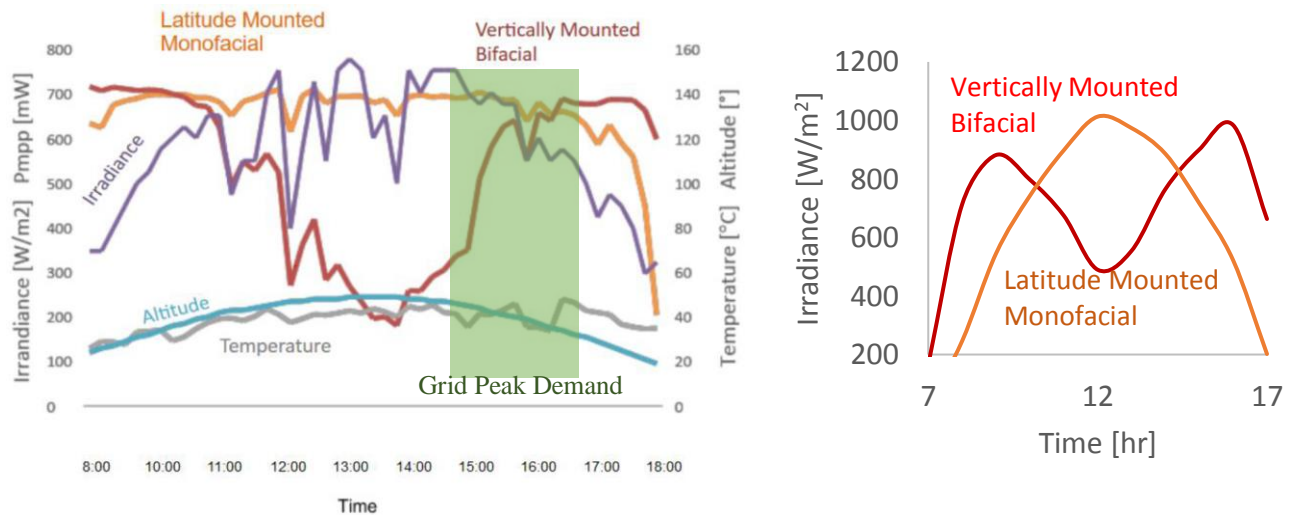
Figure 6. (a) Example of data obtained for a latitude-mounted monofacial photovoltaic (PV) module (Orange) compared to a vertically-mounted bifacial PV module (Red) for October 15, 2017. Main grid peak demand happens between 2 and 4 PM. (b) Modeling of irradiance reaching a latitude-mounted monofacial and a vertically-mounted bifacial PV for October 15, using typical meteorological year data (TMY3).

Vertically-mounted bifacial solar modules can have gains over monofacial systems anywhere in the world, with albedo values as low as 0.05 to 0.3 depending on the location [23]. The gain from optimizing these bifacial systems has also been studied and were shown to be as high as 40% compared to monofacial systems [24]. Meeting the electric demand uniformly through the day could be achieved using both latitude-mounted monofacials and vertically-mounted bifacials, make this combination attractive for stand-alone systems or for their application in solar arrays. As another option, a light-management system could be designed to improve or level-out the vertically-mounted bifacial panel response through the day, which is what chapter 2 will cover.

Chapter 2: Holographic System Design for Vertically-Mounted Bifacials

Vertically-mounted panels can produce more power during high-demand early-morning and late-afternoon periods without the need for tracking. This report proposes the use of a holographic optical element (HOE) designed to provide spectral and spatial light-management to improve the production of vertically-mounted bifacial panels when the sun's position is close to the noon position (+- 10° from the maximum zenith angle) (Figure 7). The parameters for this HOE-panel combination, referred to as a "T-cap", can be seen in Figure 8.
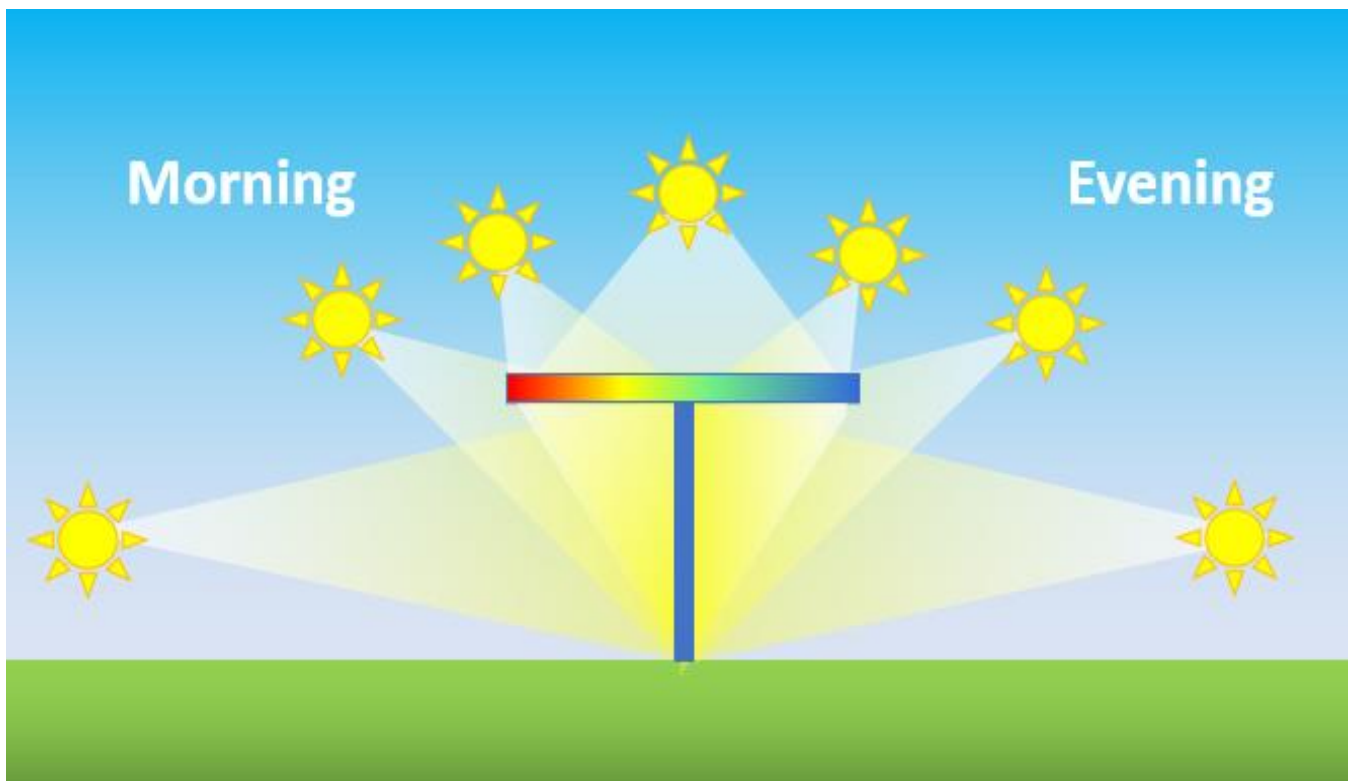
Figure 7 - Holographic optical element, placed horizontally on top of a vertically-mounted bifacial panel, forming a "T-cap".

Holographic optical elements can have broad angular-bandwidths, which is helpful for non-tracking solar systems [25]. They are recorded into a photosensitive material with two incident light propagation beams. The resulting hologram will have a specific grating vector K with a grating period Λ_x, depending on the beams' incident angles and wavelengths. Due to Bragg-matching with the grating vector recorded in the HOE, if the light's incident angle varies upon reconstruction, the peak diffraction efficiency and diffraction angle will also vary (Figure 8b). This variation must be taken into consideration when designing for a non-tracking solar system, since the sun will change positions throughout the day. The spectral content of incident sunlight also varies over the course of the day as the air mass varies. However, even more importantly for a module application, the spatial location of the diffracted spectra will change as the sun moves through the sky. Calculating the specific spectra at each cell of a module is necessary with this system, since the cell's generated current will depend on the spectral content reaching it.
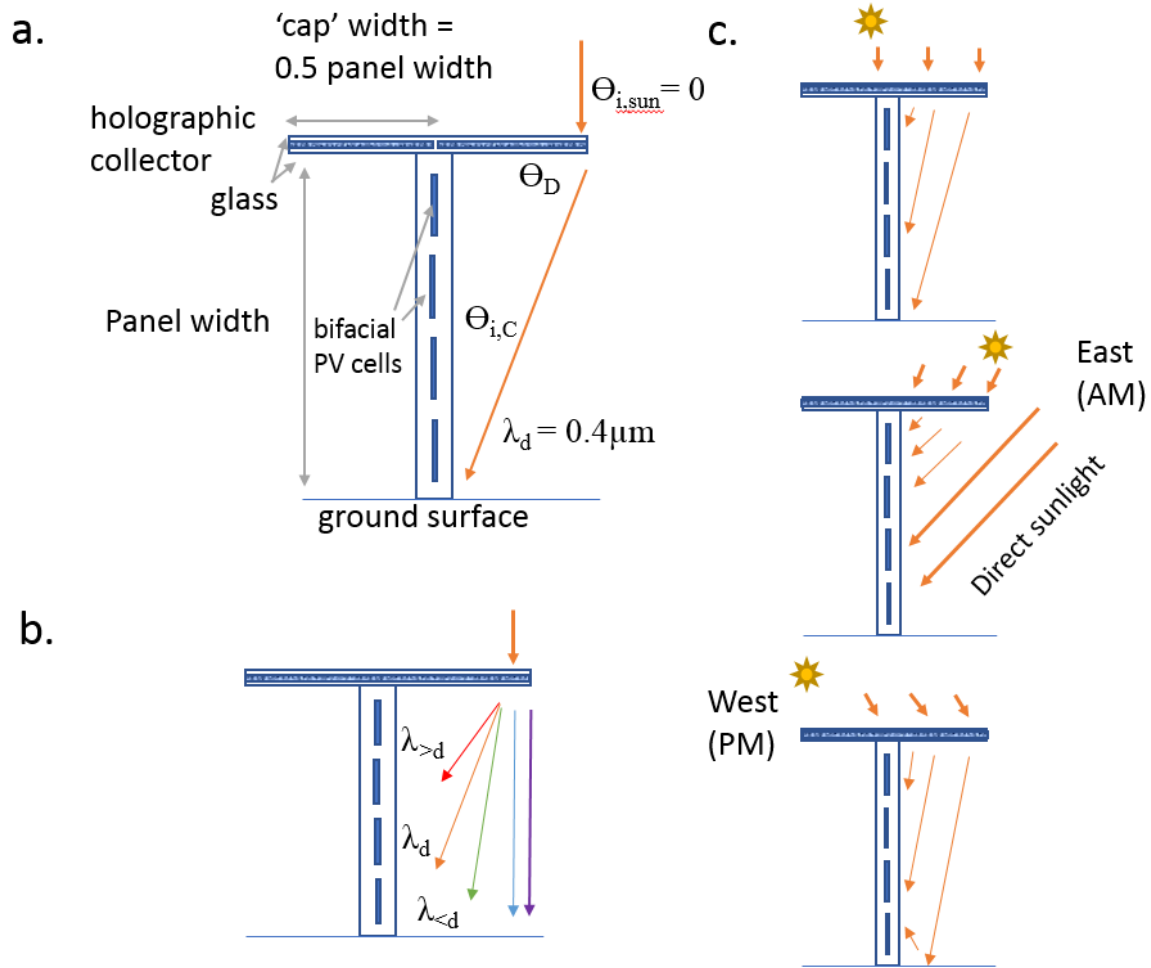
Figure 8 - (a) Diagram of the "T-cap," a vertically-mounted bifacial solar module with a holographic optical element (HOE) on top. The sun's incident light into the HOE will be diffracted by an angle Θ_D towards the panel. (b) Diffracted light is wavelength dependent. Wavelengths outside of the diffraction bandwidth (200 nm around peak diffraction wavelength) will not be affected by the grating. (c) Depending on the sun's incident angle, the angular response of the grating will vary. Both the wavelength and the angular diffraction response must be considered and can be used to optimize the grating design for the T-cap

The holographic element is positioned with the fringes parallel to the North-South axis, so that the system will be insensitive to seasonal changes in altitude. The HOE is designed to be the same on both sides of the panel, but with a 180° rotation in the grating vector around the z-axis (Figure 9), achieved simply by rotating the holographic recording material 180° during the hologram fabrication process.

20

This rotation will direct light from both sides of the cap (West and East) towards the panel for incident

sun angles of $\Theta_{i,sun}= 0°$

a.

b.
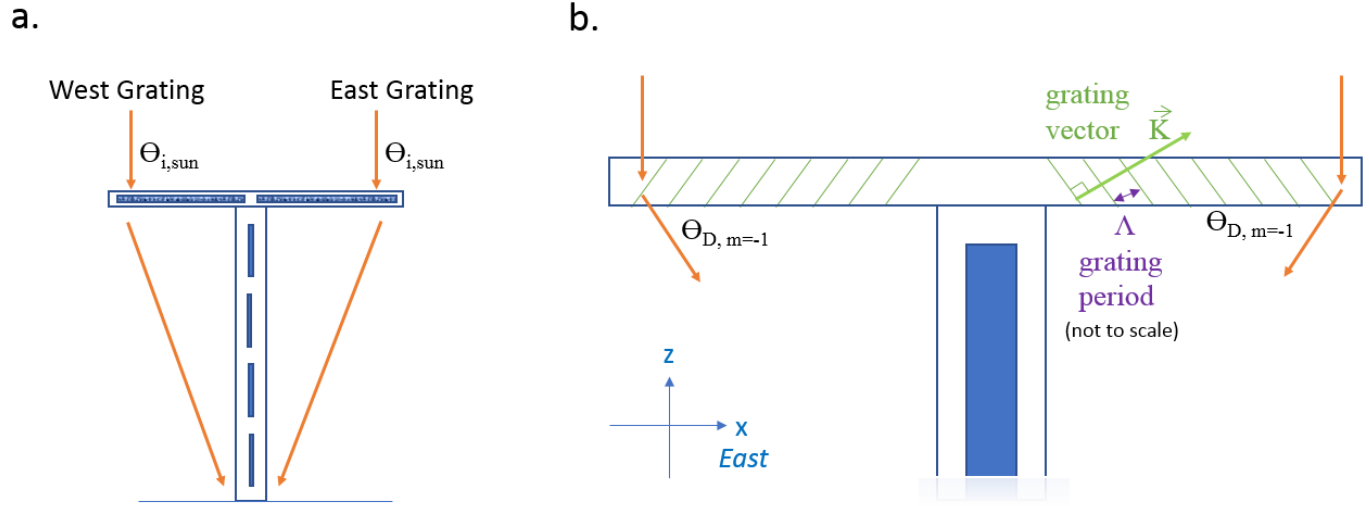
Figure 9 - (a) Grating placement to the West and East side of the panel. (b) Fringes are parallel to North-South axis. The diagram shows the grating vector K $\vec{}$, the grating period Λ and the first diffraction order for both the West and East gratings (not to scale).

The length of the holographic optic element relative to the width of the panel determines

the diffraction angle needed at the edge of the T-cap. For this paper a form factor of 0.5 has

been chosen, such that the panel is twice the width of one side of the HOE. For this geometry,

the diffracted light from the edge of the T-cap will be directed to the bottom of the panel with

a diffraction angle of $\Theta_D = 26.56°$. The wavelength diffracted to the bottom of the panel is 0.4

μm. The maximum diffraction efficiency for the grating will occur at 0.7 μm. The design

choices for the system and grating are summarized in Table 2.

Table 2 - Hologram Design Parameters

Design Wavelength (edge of HOE to bottom of panel)	0.4 μm
Form-factor T-cap (width HOE/width panel)	0.5
Incident Angle (Θ_i)	0°
Diffraction Angle (Θ_D)	26.56°
Λ_x Grating Period x	0.896
Λ_z Grating Period z	3.19
Hologram Thickness	5 μm
Hologram Material	DCG
Index of Refraction	1.52
n1	0.02
Incident Angles evaluated	±90
Wavelengths evaluated	0.3 - 1.2 μm

The grating was evaluated using Rigorous Coupled Wave Analysis in the RSOFT simulation software[26]. The diffraction orders m=+1,-1,-2,-3 were simulated for in-plane input angles ranging from $\pm90°$ relative to surface normal. Figure 10 shows the resulting diffraction efficiency for a couple input angles, at first order (m=-1). The resulting spectral bandwidth is of 200 nm for normal incident light, peaking at the design wavelength of 0.700 μm with diffraction efficiency of 95%.
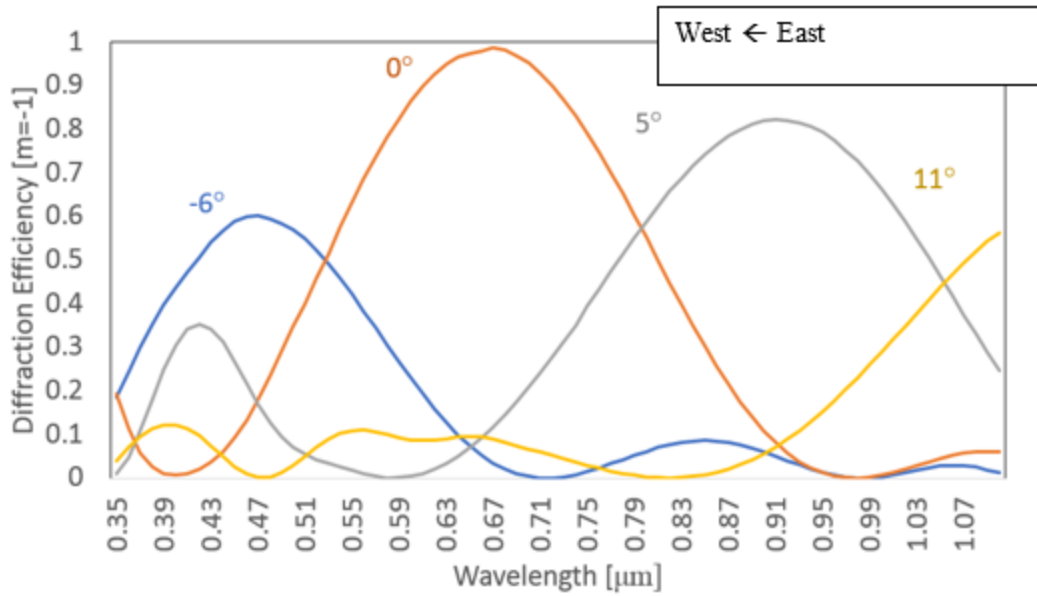
Figure 10 - (Left) Values used for the grating design. (Right) Diffraction efficiency for first order (m=-1) at incident light angles of -6°, 0°, 5°, and 11°, generated in RSOFT. As the sun moves from east to west the grating's efficiency will vary by the incident angle.

Two different and independent methods are presented in this report for evaluating the T-cap system: 1) raytracing through holographic transfer relations, and 2) full reverse-raytrace system. They are evaluated in Chapter 3 and 4 respectively.

Chapter 3: Modeling with Holographic Transfer Relations

3.1 Method

The first method used for evaluating the T-cap is a simple geometrical raytrace, which assumes a hologram plane, and evaluates rays going through a specific coordinated (as an example, the one marked with the green dot in Figure 11), and to a location on an image plane a distance z_i away.
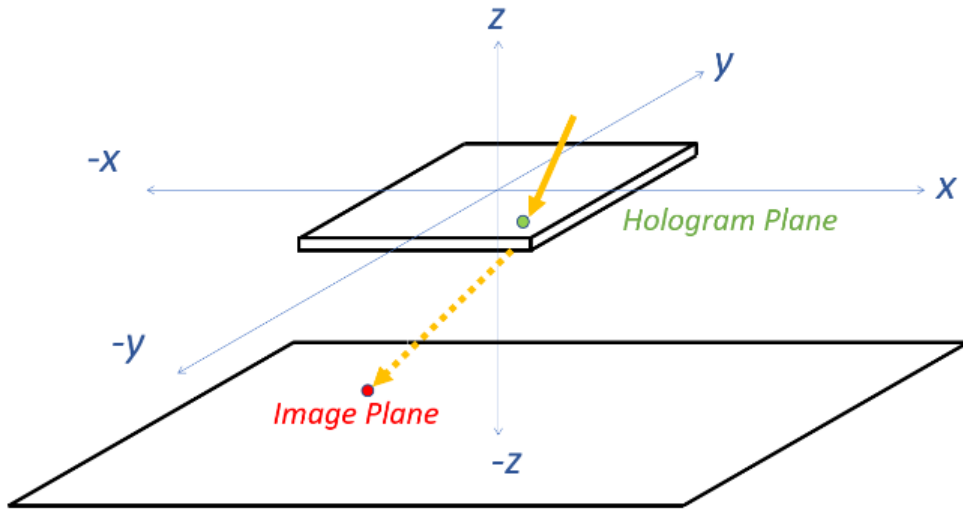
Figure 11 - Hologram and image plane location for holographic transfer relations algorithm.

The hologram is recorded at a wavelength λ_1, with reference and object beam propagation vectors that have direction cosines (l_o, m_o, n_o) and (l_r, m_r, n_r). The grating can be evaluated at any reconstruction wavelength λ_2 and angles determined by direction cosines l_p and n_p. For these conditions the image direction cosines and image intercepts are:

$$l_i = (l_o - l_r)^{\lambda_2}/_{\lambda_1} + l_p \tag{6}$$

$$m_i = (m_o - m_r)^{\lambda_2}/_{\lambda_1} + m_p \tag{7}$$

$$r_i = \frac{z_i}{(n_o - n_r)^{\lambda_2}/\lambda_1 + n_p}$$ (8)

$$x_i = r_i * l_i + x_h$$ (9)

$$y_i = r_i * m_i + y_h$$ (10)

As can be seen in Figure 12, a ray hitting the cap at (xh, yh, 0) is related to a point on the image plane (xi, yi, zi), which is traditional used for ray tracing.
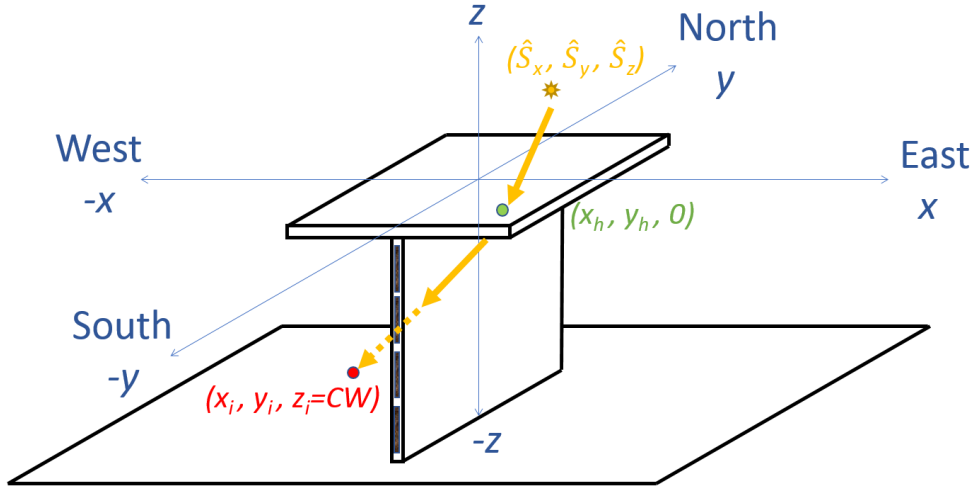
Figure 12 - Coordinate system and parametric ray-trace transfer coordinates.

The ratio of rays intercepting the panel with and without the HOE is a simple metric of performance:

$$HOE_{gain} = \frac{\#Rays_{HOE@panel}}{\#Ray_{@panel}}$$ (11)

where $\#Rays_{HOE@panel}$ are rays that reach the vertically-mounted bifacial module when the hologram is present, and $\#Ray_{@panel}$ are rays that reach the vertically-mounted bifacial module when there is no hologram. For calculating $\#Ray_{@panel}$ the sun's vector can be propagated through the same coordinate without intercepting a HOE, modifying equations 8-10 such that:

25

$$x_{i,s} = \frac{z_i}{n_p} * l_p + x_h \tag{12}$$

$$y_{i,s} = \frac{z_i}{n_p} * m_p + y_h \tag{13}$$

1.2 Results

The sun's azimuth and zenith angles were calculated using the National Renewable Energy Laboratory (NREL) Solar Position Algorithm [27] for Tucson, AZ (latitude 32.133°, long=-110.95°, elevation=777m). The sun's cartesian coordinates were calculated at 5-minute intervals over a full year:

$$\begin{pmatrix} \hat{S}_x \\ \hat{S}_y \\ \hat{S}_z \end{pmatrix} = \begin{pmatrix} \cos\theta_{alt}\,\cos\theta_{azm} \\ \cos\theta_{alt}\,\sin\theta_{azm} \\ \sin\theta_{alt} \end{pmatrix} = \begin{pmatrix} l_p \\ m_p \\ n_p \end{pmatrix} \tag{14}$$

Figure 13 shows the top view of the image plane, with the bifacial photovoltaic panel of 10 cm height at x=0. Also shown are rays that hit the image plane after passing through a cap at point $x_h =$ 5cm, y_h=10cm, without a hologram for different positions of the sun. Rays through the (x_h, y_h) position on the cap are sampled at 5-minute intervals and the intercept points on the image plane are shown. Since the sampled coordinate is on the East side of the vertically-mounted panel, rays at the left of the y-axis reach the panel, counting towards $\#Ray_{@panel}$. For this day, no rays going through the sampled coordinate reach the panel between the hours of 11 to 1 PM.
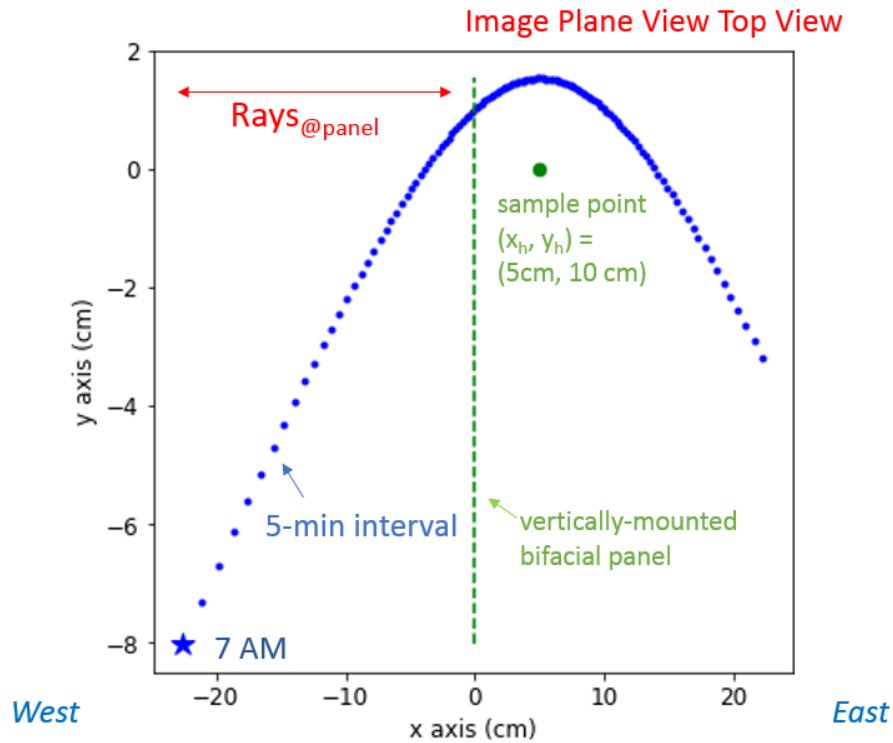
Figure 13 - Top view of the image plane. The sampled point in the hologram plane (without hologram) is marked in green. The rays reach the image plane at the blue-points, each one representing a 5-min interval for the day sampled, June 21st. Rays to the left of the y-axis reach the panel and count towards Rays@panel.

Repeating the analysis with the holographic cap in place shows that at the same entry point on the cap a total of 270 rays intercept the vertically-mounted module between 11 am and 1 pm, for a wavelength of 0.4 µm (Figure 14). The ray-intercept for noon for this wavelength is at the bottom edge of the solar panel, marked by the green star coincident with the axis x=0. Through the whole day, the improvement in the number of rays reaching the module with the holographic optical element is of 47%.
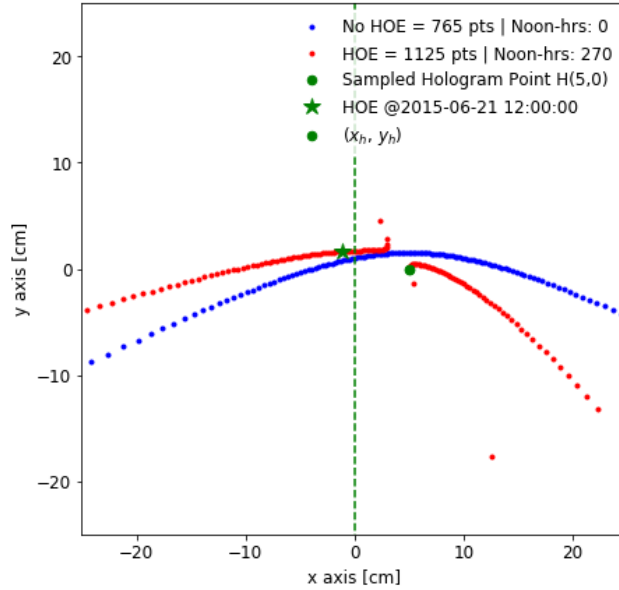
Figure 14 - Comparison of 5-min interval rays incident in the image plane with and without the hologram, for λ=0.4 μm for one day (June 21st). Ray for 12 pm is marked with a green star. Points to the left of the green axis reflect rays incident on the vertically-mounted module.

Results at λ=0.7 μm can be seen in Figure 15 (a), and (b) shows results for different sample points on the T-cap. For sample points closer to the panel (green doted line), more rays between 11-1 PM hours will reach the module.
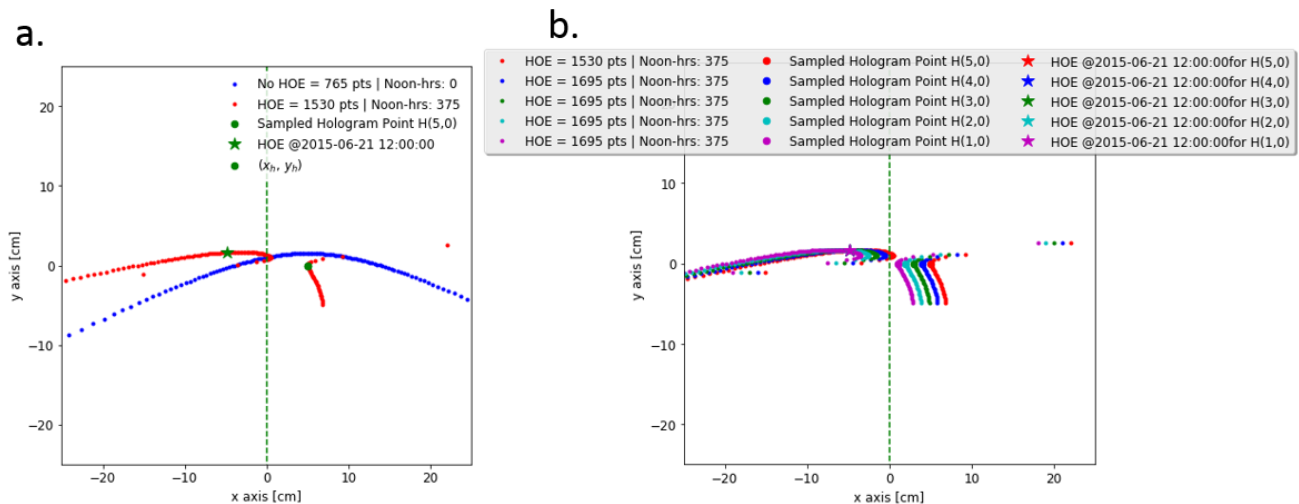
Figure 15 – Rays incident in the image plane and in the panel with and without the hologram, for λ=0.7 μm. (b) Rays incident in the image plane for different sampled points in the hologram.

Figure 16 shows the performance with and without a hologram for a one year time period. With the hologram, the number of rays reaching the module significantly increases. To visualize the improvement of the grating, rays before noon are colored in red and after 12 PM in green.

$HG_{year} = 511380/239565 = 113\%$, $HG_{year@noon-hrs} = 136875/5940 = 2204,\% \lambda = 0.7\ \mu m$

Legend:
- No HOE = 239565 pts | Noon-hrs: 5940
- HOE Morning = 317445 NO CAP:239565 pts
- HOE Afternoon = 193935 NO CAP:0 pts
- Sampled Hologram Point x_h, y_h (5,0)
- ★ HOE @2015-06-21 12:00:00
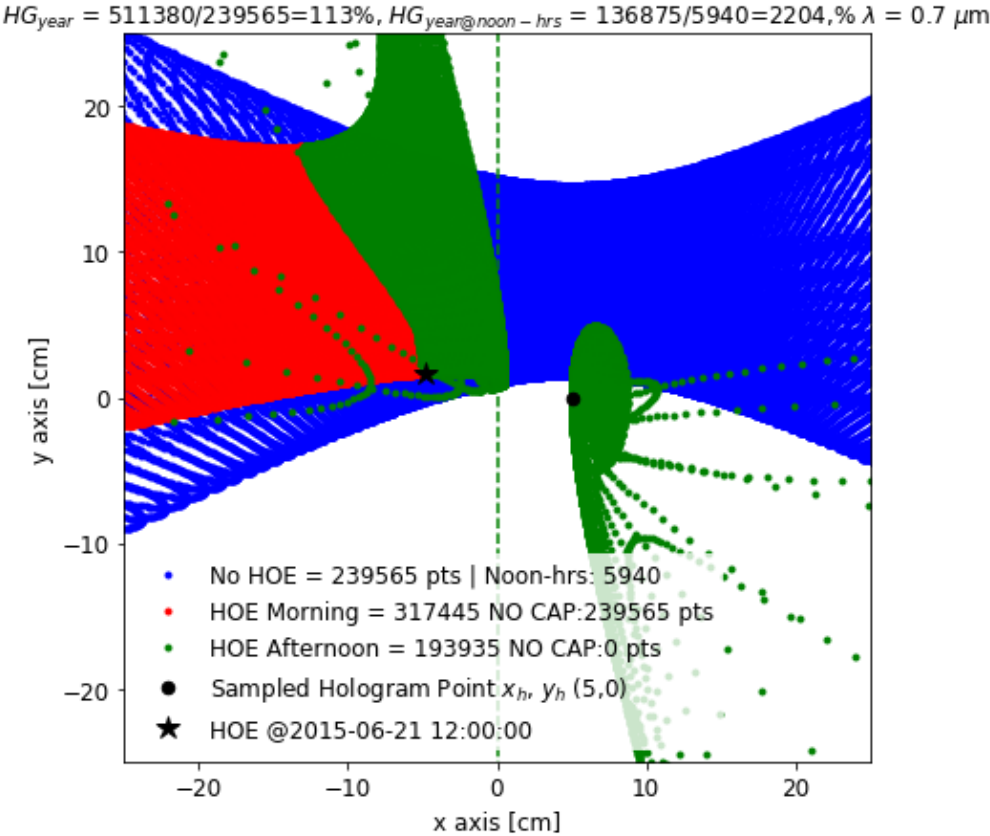
Figure 16 - Results for Holographic Transfer Relations for a whole year. Each point represents 5 min interval. Before- and after-noon rays are marked by red and green points, respectively.

The method explored in this chapter provides an idea of the irradiance distribution on the vertically-mounted panel, but it does not consider the hologram efficiency, the sun's irradiance, diffuse light and/or reflections from the ground, thus the real irradiance or improvement in the plane is not known. A more complete model is needed, as described and evaluated in Chapter 4.

Chapter 4: Reverse Raytrace Modeling

To calculate the irradiance received at the panel, a simulation tool was developed using the open-source software packages SMARTS[28], GenCumSky[29], and the raytracing software FRED[30]. SMARTS is used to simulate direct and diffuse spectra at a specific time and geographical location, considering the local atmosphere composition. Based on the sky-model by Perez [31], GenCumSky generates sky-luminance distributions using typical meteorological year data (TMY3) [18]. Both SMARTS spectra and the sky-luminance distribution from GenCumSky were implemented using reverse-raytrace analysis in FRED to obtain the irradiance reaching the front and rear surfaces of the bifacial solar panel. The algorithm is described in Figure 17.
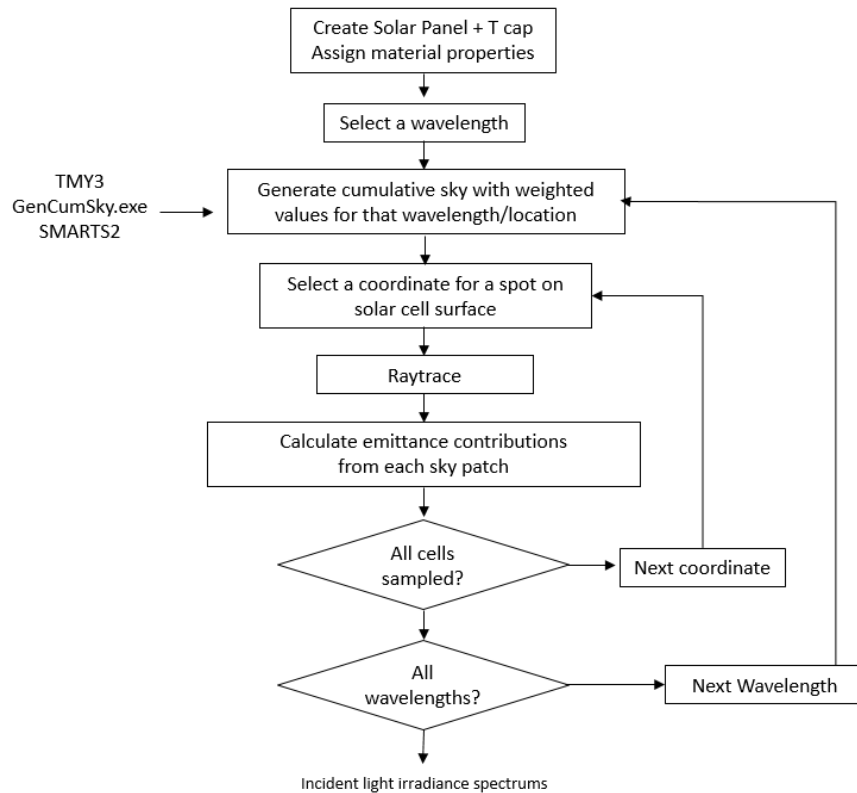
Figure 17 - Flow chart of the script to run FRED software and calculate incident light irradiance spectrum on the bifacial solar cell surface.

The ratio of the irradiance received by the bifacial panel with the cap (E_{T-cap}) to the irradiance of only the vertically-mounted bifacial module without the cap (E_{VMB}) quantifies the gain from using the holographic optical element in the system:

$$HOE_{gain} = \frac{E_{T-cap}}{E_{VMB-EW}} \qquad (15)$$

The irradiance received will depend on the geometry of the system, the sun position, the ground albedo, and the available direct and diffuse light at the time of evaluation. For the case of the system with the T-cap, the diffraction efficiency and grating period of the HOE will also influence the irradiance. The annual gain can be calculated by summing the irradiance for a year at each hour (a total of 8760 hours):

$$HOE_{annual-gain} = \frac{\sum_1^{8760} E_{T-cap}}{\sum_1^{8760} E_{VMB-EW}} \qquad (16)$$

The following sections will describe the raytrace implemented in more detail, and then results are presented.

4.1 Cumulative Sky

Robinson and Stone proposed in 2004 a way to describe the sky's luminance dividing it into patches [29]. Each patch gets assigned a radiance value following the Perez Model, such that patches closer to the sun have a higher value than others. The sun can be modeled discretely or added into the closest patch. Using typical meteorological year data as input for the Direct and Diffuse (DNI and DHI) values, this model can also take into consideration weather patterns, when coupled with typical meteorological year data. It can be used to model a single hour or any period (day, month, year, etc.) by adding up every hour to a create a "cumulative" sky (Figure 18).
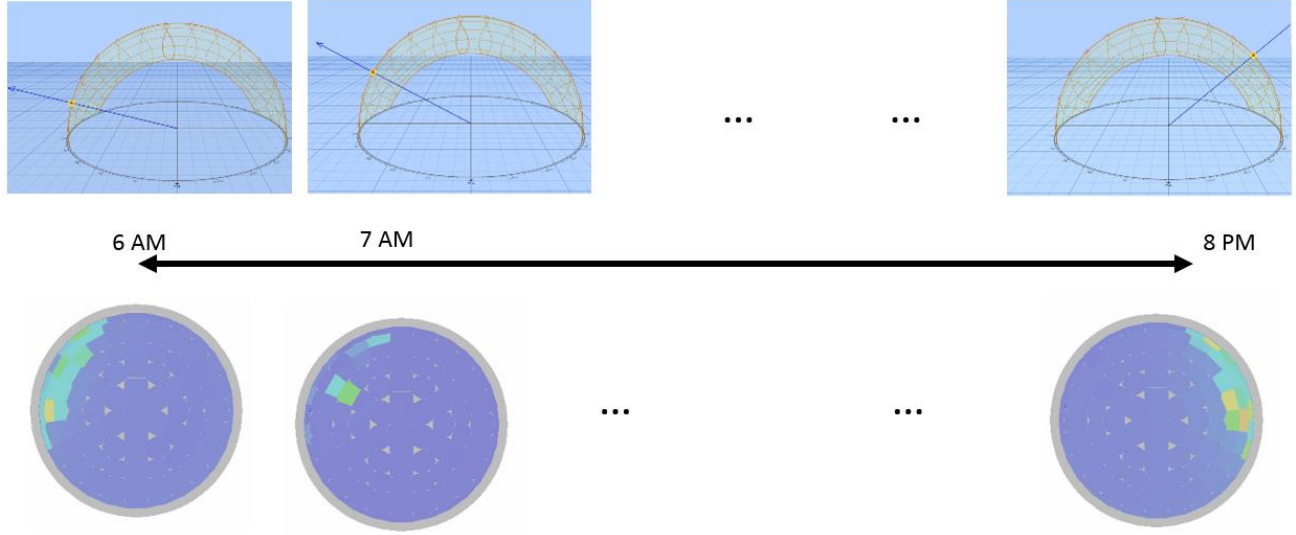
Figure 18 - A distribution of radiance for a sky-hemisphere can be calculated for each hour using the Perez model, and added for a cumulative sky encompassing any period (day, month, year).

4.2 Sky-Luminance Distribution by Wavelength

The absolute diffuse radiance for each sky patch i, R_i, is calculated following the model for instantaneous luminance distribution described in [29]. The radiance value for the patch in which the sun is located ($R_{i,s}$) is increased by the radiance value.

Direct and diffuse spectra are calculated with SMARTS2 for the 8760 hours in the year. The spectral irradiance is integrated to calculate the total ideal direct irradiance $I_{D,ideal}$ and total ideal diffuse irradiance $I_{dh,ideal}$:

$$I_{D,ideal} = \sum_{\lambda=280nm}^{4000nm}(\lambda_i - \lambda_{i+1})I_D(\lambda) \tag{17}$$

$$I_{dh,ideal} = \sum_{\lambda=280nm}^{4000nm}(\lambda_i - \lambda_{i+1})I_{dh}(\lambda) \tag{18}$$

Normalized spectra $I_{D,\lambda,norm}$ and $I_{dh,\lambda,norm}$ can be calculated by dividing the spectra at each wavelength by the $I_{D,ideal}$ and $I_{dh,ideal}$ values:

32

$$1 = \sum_{\lambda=280nm}^{4000nm}(\lambda_i - \lambda_{i+1})I_D(\lambda)/I_{D,ideal} \tag{19}$$

$$1 = \sum_{i=1}^{p}(\lambda_i - \lambda_{i+1})I_{dh}(\lambda)/I_{dh,ideal} \tag{20}$$

$$I_{D,norm}(\lambda) = I_D(\lambda)/I_{D,ideal} \tag{21}$$

$$I_{dh,norm}(\lambda) = I_{dh}(\lambda)/I_{dh,ideal} \tag{22}$$

The radiance at each wavelength for the sun patch can be calculated by multiplying the normalized spectra from eq. 21 by that patch's radiance:

$$R_{i,S}(\lambda) = \left(I_{D,norm}(\lambda)\right)R_{i,S} \tag{23}$$

For the rest of the R_i patches (except $R_{i,S}$), the radiance at each wavelength can be calculated by multiplying the normalized diffuse spectra from eq. 22 by each patch's radiance:

$$R_i(\lambda) = \left(I_{dh,norm}(\lambda)\right)R_i \tag{24}$$

The cumulative radiance (Whm-2Sr-1) / luminance (lmh.m-2Sr-1) for each wavelength a given period is simply the aggregation of the instantaneous results within these patches.

$$R_{i,year}(\lambda) = \sum_{t=1}^{8760} R_i(\lambda,t) \tag{25}$$

4.3 Raytrace Modeling

The vertically-mounted bifacial module and holographic optical element were modeled with the FRED Optical modeling software. The holographic optical element width is half of the panel height (5cm and 10 cm, respectively). Standard SCHOTT glass was assigned for the panel glass and the glass surrounding the gratings (n=1.54, reflectivity of 4%). An infinite sky surface was defined (5000 times greater than the T-cap), and the values were assigned for each wavelength emittance calculated from

the method described previously in this chapter. The ground albedo was set to be a coating with 62% reflectivity (Figure 19), with Lambertian scattering (96%) properties. The panel and grating were assumed to be infinite in the N-S axis.
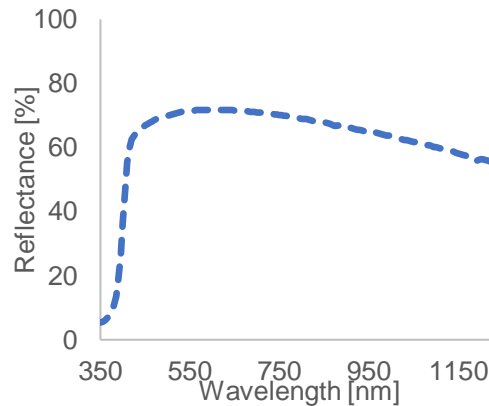
Figure 19 - Henry Tropi-Cool average reflectance, measured with a Lambda 1050 UV/VIS photospectrometer.

A reverse-raytrace routine was implemented in FRED to sample the spectral irradiance received at specific locations in the vertically-mounted bifacial module from the sky-hemisphere (Figure 20). Reverse raytrace is an application of radiative transfer theory [32]. The advantages of using reverse-ray trace is reduced simulation time[6]. The method uses a source at the desired sampling point that emits rays into a half-hemisphere (2π). The number of rays reaching each sky patch is multiplied by that sky patch's radiance value, and the contributions from all sky patches are added to calculate the irradiance at the point being sampled.
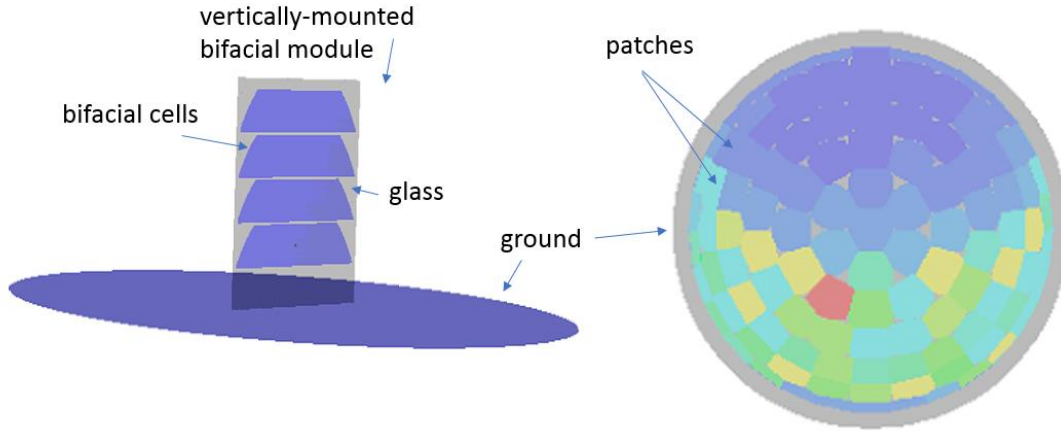
Figure 20 - Vertically-mounted bifacial module and sky-hemisphere modeled in FRED.

4.4 Raytrace Results

Figure 22 shows results for two different hours on June 21st. Improvement is visible in the wavelengths of interest between 380nm to 1100 nm, corresponding to the bifacial cell's silicon spectral responsivity. There is notable improvement around 700 nm, the wavelength for which the hologram is designed. The spectra with and without the T-cap is shown for different positions along the module in Figure 22. The gain varies with the location sampled on the panel. The improvement or gain as defined in equation (15) reaches as high as 30%, but also varies spatially and by wavelength.
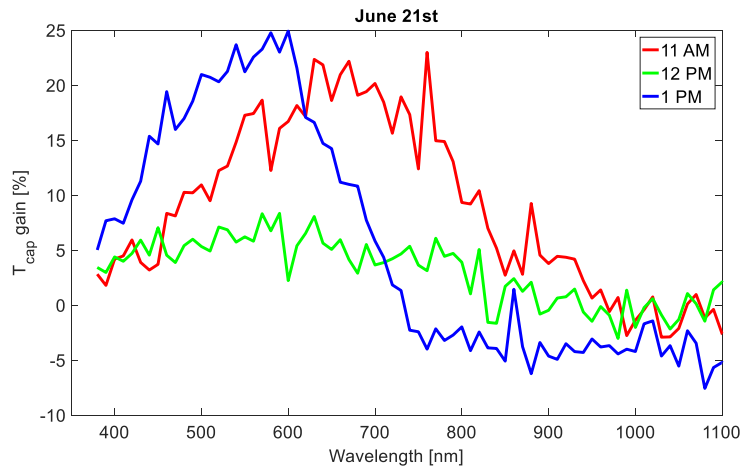
Figure 21 - T-cap gain with respect to a glass cap for 11AM, 12 noon, and 1 PM as a function of wavelength for June 21 from TMY 3 illumination data for Tucson, AZ.

11 AM

Spectra   With cap   **** With No cap

$$HOE_{gain,\lambda} = \frac{E_{T-cap}}{E_{VMB-EW}}$$

Spectral Irradiance [Wm^{-2}nm^{-1}]

$HOE_{gain,\lambda}$ [%]

wav [nm]

wav [nm]

12 AM

Spectra   With cap   **** With No cap

$$HOE_{gain,\lambda} = \frac{E_{T-cap}}{E_{VMB-EW}}$$

Spectral Irradiance [Wm^{-2}nm^{-1}]

$HOE_{gain,\lambda}$ [%]

wav [nm]

wav [nm]
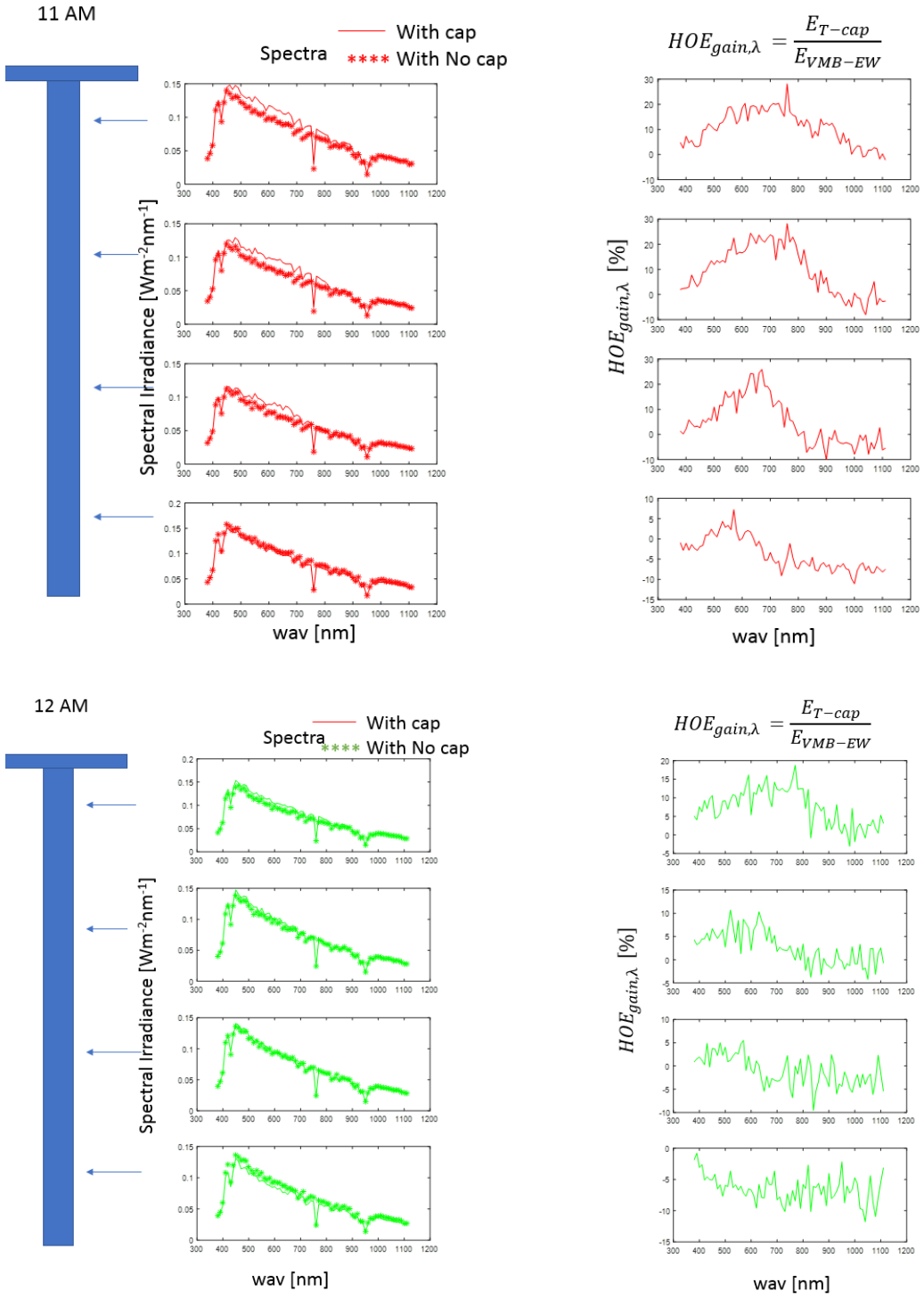
Figure 22 - Spectra received at different positions in the solar panel with and without the Holographic Optical Element.

36

The spatial distribution of the spectra with the grating needs to be further evaluated to better understand the current production of each cell and the overall performance of the panel with the holographic cap. The average hourly gain in spectral irradiance is plotted in Figure 23. There are many elements that play into the results presented, like the weather patterns, or the fact that solar zenith doesn't happen at exactly 12:00 pm (Figure 24). This day modeled is cloudy before and around noon, with approximately 50% diffuse-to-direct content. However, even under this highly-diffuse scenario there are gains from having the hologram. Solar noon for this day (June 21st, 2018) occurs at 12:30pm.
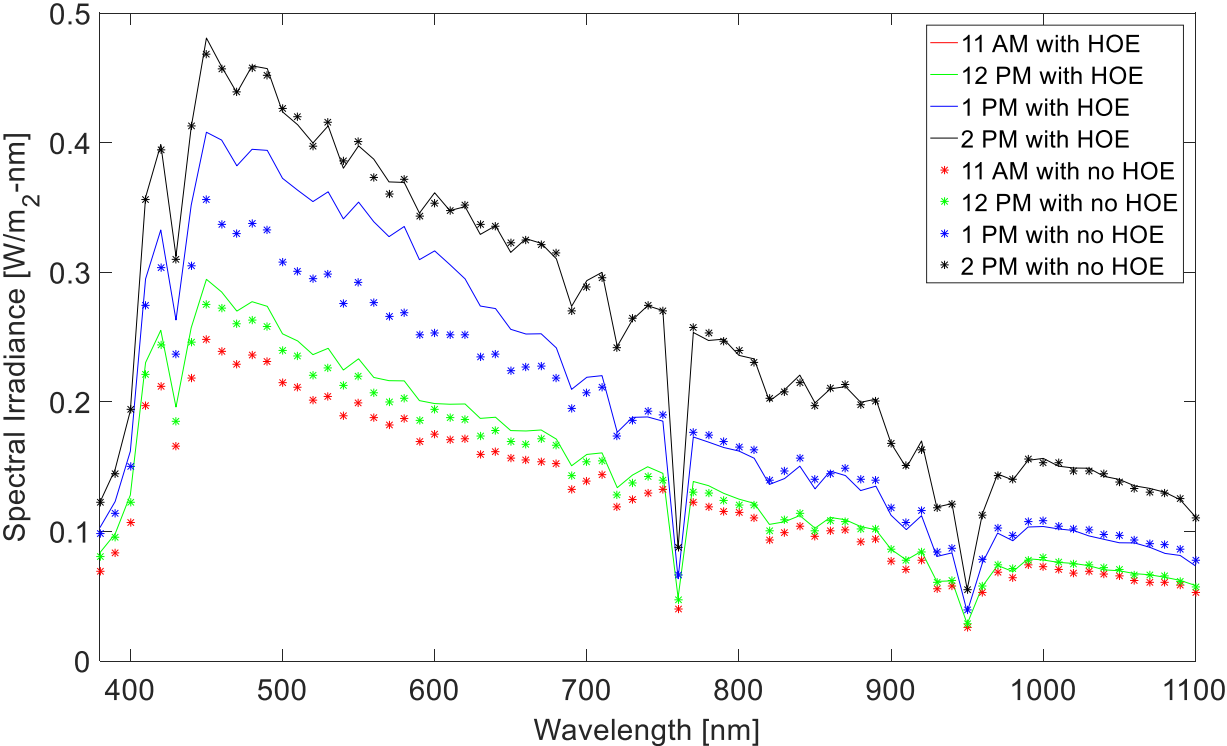
Figure 23 - Averaged spectra received with and without the HOE at different hours for June 21st.
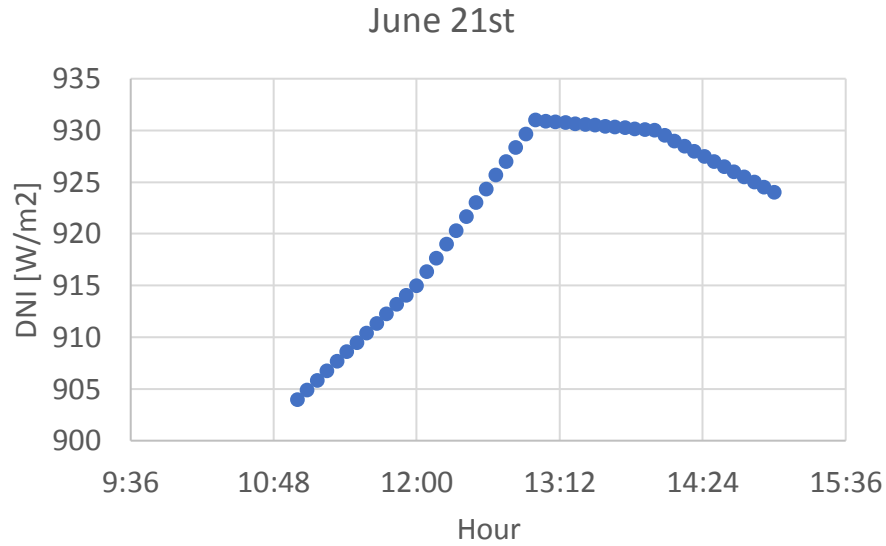
Figure 24 - June 21st, hourly interpolated DNI according to typical meteorological year data (TMY3).

The accumulated yearly spectral irradiance reaching the panel was calculated at four points on the front and rear (east and west) of the vertically-mounted module, with and without the holographic optical element. The improvement of this accumulated irradiance, in the wavelengths of the silicon spectrum response (380-1100 nm) was measured using equation 16 and is summarized in Table 3.

Table 3-Yearly irradiance-collection improvement using Holographic T-cap

	$HOE_{annual-gain}$
Vertically-mounted module only	--
With T-cap	**0.5%**
Glass losses	**-0.03%**

4.2 Re-design considerations

The assumptions made for the design of the hologram were $\Theta_{i,sun} = 0°$, with no variation in the diffraction efficiency of the hologram for out-of-plane angles. The tilt of the T-cap is $0°$ and the beam radiation reaches its surface at the lowest angles of incidence in the summer when the sun is at its highest altitude (Figure 25).
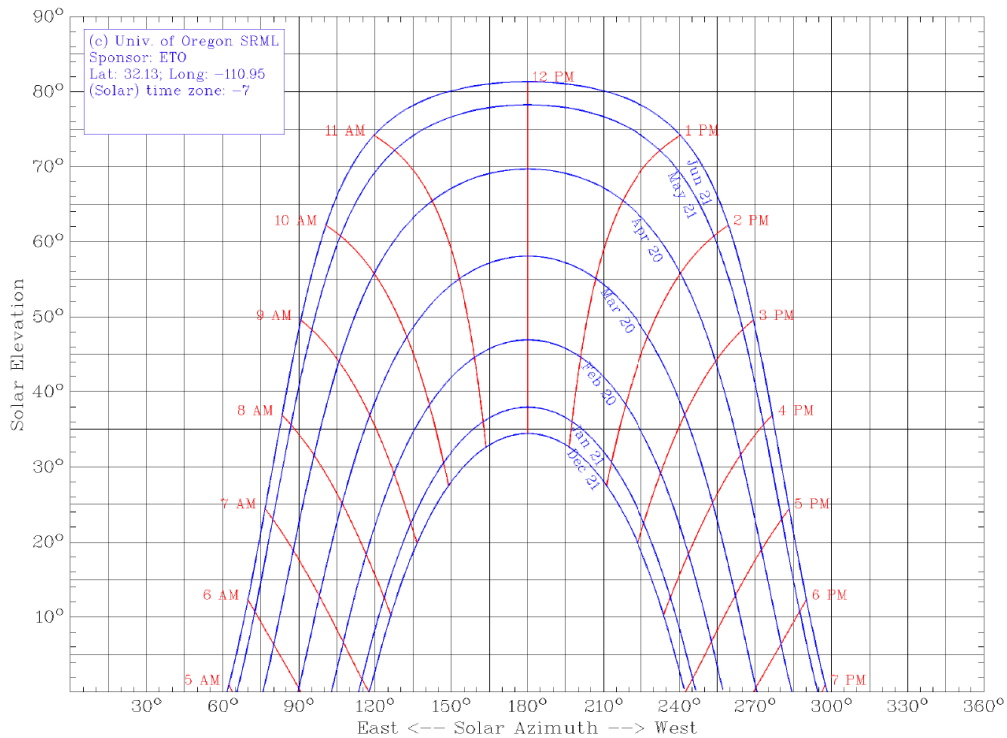
Figure 25 - Solar Azimuth versus Solar Elevation plot for Tucson, AZ, generated using the University of Oregon's Solar Position Calculator [http://solardat.uoregon.edu/SolarPositionCalculator.html].

Following the procedure established by Slauch et al [33], the overall energy versus angle of incidence was calculated for the T-cap and can be seen in Figure 26. The energy fraction received at each angle considers beam and diffuse energies taken from typical meteorological year data set in the National Solar Radiation Data Base [18] and interpolated to 1 min intervals. An isotropic sky-model is assumed for the diffuse energy contribution. The angle of incidence (Θ_{AOI}) is calculated using the

39

National Renewable Energy Laboratory (NREL) Solar Position Algorithm[27] for Tucson as a function of module tilt and azimuth angles. At 30 degrees tilt (close to latitude for Tucson), the angle of incidence of beam radiation with the module is lowest near the equinoxes and the energy fraction peaks at 23 degrees.
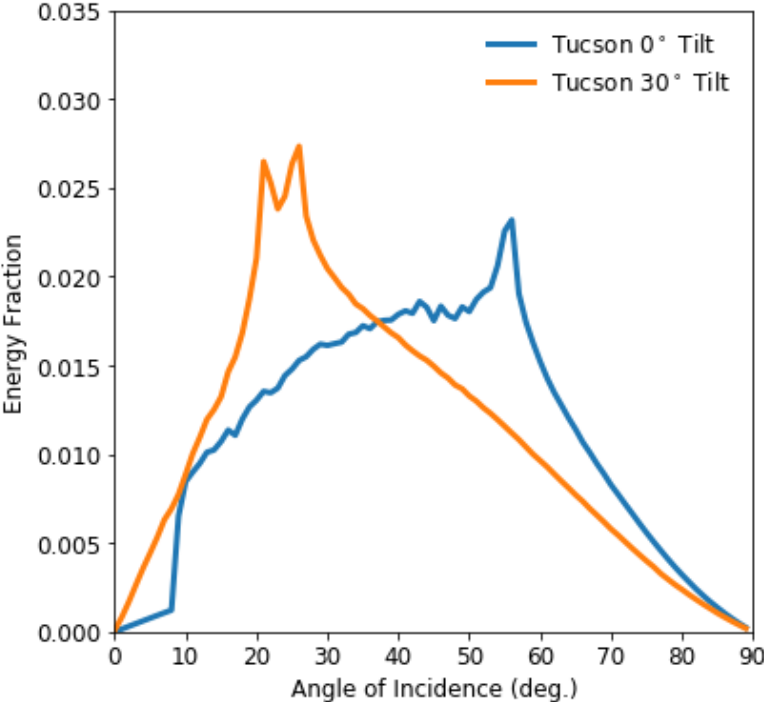
Figure 26 - Overall energy versus angle of incidence for a surface at 0° tilt (blue) and at 30° tilt (orange) for Tucson, AZ. For the T-cap, 0° tilt is the tilt of the grating.

Designing and testing other grating design parameters are needed to optimize the system. Particularly, the decision of diffracting λ=0.4 µm from the edge of the hologram to the bottom of the vertically-mounted module is something that needs to be analyzed, since perhaps other design parameters might yield better overall-yearly results.

Conclusions

The use of a holographic optical element has been proposed to improve the light-collection and thus energy-production of vertically-mounted bifacial photovoltaic modules around solar zenith. A grating has been designed for the system, with maximum diffraction efficiency at 0.7 µm and a diffraction bandwidth of 200 nm in ammonium dichromate gelatin. Two independent methods have been presented to calculate the improvement of using this grating with the vertically-mounted bifacial module. Method one uses holographic transfer relations to calculate the increase in the number of sun rays at the PV module due to the holographic optical element. A 113% increase in rays reaching the panel is predicted for the year when evaluating points at the edge of the holographic grating, however this method assumes 100% hologram efficiency and does not consider Fresnel losses, so it does not give an accurate sense of the degree of improvement. As a second method a reverse-raytrace has been implemented to evaluate on more detail the performance of the grating, considering Fresnel reflections, and ground reflectance and scattering. For spectra between 380 and 1100nm, 0.5% more irradiance is expected for the whole year with the grating. Future steps include optimization of the grating, more detailed modeling for other sample days in the year, and recording the hologram grating for gathering test-data with a module.

References

[1]   G. R. Newsham and B. G. Bowker, "The effect of utility time-varying pricing and load control strategies on residential summer peak electricity use: a review," *Energy Policy*, vol. 38, no. 7, pp. 3289–3296, 2010.

[2]   A. Cuevas, "The early history of bifacial solar cells," in *Proc. of the 20th European Photovoltaic Solar Energy Conference*, 2005.

[3]   T. Dullweber, H. Schulte-Huxel, H. Hannebauer, S. Blankemeyer, U. Baumann, S. Schimanke, R. Witteck, M. Köntges, and R. Brendel, "Bifacial PERC+ solar cells: status of industrial implementation and future perspectives," in *bifiPV2017 Workshop, Konstanz,* 2017.

[4]   L. Yang, Q. H. Ye, A. Ebong, W. T. Song, G. J. Zhang, J. X. Wang, and Y. Ma, "High efficiency screen printed bifacial solar cells onmonocrystalline CZ silicon," *Prog. Photovoltaics Res. Appl.*, vol. 19, no. 3, pp. 275–279, 2011.

[5]   C. W. Hansen, R. Gooding, N. Guay, D. M. Riley, J. Kallickal, A. Asgharzadeh, B. Marion, F. Toor, and J. S. Stein, "A Detailed Model of Rear-Side Irradiance for Bifacial PV Modules," in *44th IEEE Photovoltaic Specialists Conference. Washington, DC. SAND2017-6554 C.*, 2017.

[6]   C. Deline, S. MacAlpine, B. Marion, F. Toor, A. Asgharzadeh, and J. S. Stein, "Assessment of Bifacial Photovoltaic Module Power Rating Methodologies—Inside and Out," *IEEE J. Photovoltaics*, vol. 7, no. 2, pp. 575–580, 2017.

[7]   SEMI P V, "Group 2017 International Technology Roadmap for Photovoltaic (ITRPV. net), Results 2016 (8th Edition)." Results, 2016.

[8]   V. Fakhfouri, "Photovoltaic Devices--Part 1--2: Measurement of Current-Voltage Characteristics of Bifacial Photovoltaic (PV) Devices," 2015.

[9]   H. Schulte-Huxel, F. Kiefer, S. Blankemeyer, R. Witteck, M. Vogt, M. Köntges, R. Brendel, J. Krügener, and R. Peibst, "Flip-Flop cell interconnection enabled by an extremely high bifaciality of screen-printed ion implanted n-PERT Si solar cells," in *Proc. 32nd European PV Solar Energy Conference and Exhibition. Munich, Germany.*, 2016, pp. 407–412.

[10]   J. E. Castillo-Aguilella and P. S. Hauser, "Multi-Variable Bifacial Photovoltaic Module Test Results and Best-

Fit Annual Bifacial Energy Yield Model," *IEEE Access*, vol. 4, pp. 498–506, 2016.

[11]   S. Ayala, C. Deline, S. Macalpine, B. Marion, J. S. Stein, and R. K. Kostuk, "Comparison of bifacial solar irradiance model predictions with field validation," *Manuscr. Submitt. Publ.*, 2018.

[12]   M. Chiodetti, "Bifacial PV plants: performance model development and optimization of their configuration," M.S. Thesis, KTH Royal Institute of Technology, Stockholm, Sweden, 2015.

[13]   C. W. Hansen, J. S. Stein, C. Deline, S. Macalpine, B. Marion, A. Asgharzadeh, and F. Toor, "Analysis of irradiance models for bifacial PV modules," in *43rd IEEE Photovoltaic Specialist Conference. Portland, Oregon. SAND2016-0803 C.*, 2016, pp. 138–143.

[14]   C. K. Lo, Y. S. Lim, and F. A. Rahman, "New integrated simulation tool for the optimum design of bifacial solar panel with reflectors on a specific site," *Renew. Energy*, vol. 81, pp. 293–307, 2015.

[15]   B. Marion, S. MacAlpine, C. Deline, A. Asgharzadeh, F. Toor, D. Riley, J. Stein, and C. Hansen, "A Practical Irradiance Model for Bifacial PV Modules: Preprint," in *44th IEEE Photovoltaic Specialists Conference. Washington, DC.*, 2017.

[16]   A. Mermoud and B. Wittmer, "Bifacial shed simulation with PVSyst," presented at Bifacial Workshop 2017, Konstanz, Germany, 2017.

[17]   P. Solar, *Design Guide for Bifacial Solar Modules*. Prism Solar Technologies, rev 2.1, 2017.

[18]   S. Wilcox and W. Marion, *Users manual for TMY3 data sets*. National Renewable Energy Laboratory Golden, CO, 2008.

[19]   F. E. R. Commission and others, "Open access same-time information system and standards of conduct," *Order*, vol. 889, 1997.

[20]   P. Denholm, M. O�Connell, G. Brinkman, and J. Jorgenson, *Overgeneration from solar energy in California: a field guide to the duck chart*. National Renewable Energy Laboratory Golden, CO, 2015.

[21]   NREL, "BifacialVF," 2018. [Online]. Available: http://github.com/NREL/bifacialvf. [Accessed: 21-May-2018].

[22]   R. Guerrero-Lemus, R. Vega, T. Kim, A. Kimm, and L. E. Shephard, "Bifacial solar photovoltaics - A technology review," *Renew. Sustain. Energy Rev.*, vol. 60, pp. 1533–1549, 2016.

[23]   S. Guo, T. M. Walsh, and M. Peters, "Vertically mounted bifacial photovoltaic modules: A global analysis," *Energy*, vol. 61, pp. 447–454, 2013.

[24]   M. R. Khan, A. Hanna, X. Sun, and M. A. Alam, "Vertical bifacial solar farms: Physics, design, and global optimization," *Appl. Energy*, vol. 206, no. September, pp. 240–248, 2017.

[25]   R. K. Kostuk, J. Castro, and D. Zhang, "Holographic low concentration ratio solar concentrators," *Front. Opt. Opt. Soc. Am.*, 2009.

[26]   Synopsys, "DiffractMOD Product Overview." 2015.

[27]   I. Reda and A. Andreas, "Solar Position Algorithm for Solar Radiation Applications."

[28]   C. A. Gueymard, "SMARTS2, A Simple Model of the Atmospheric Radiative Transfer of Sunshine : Algorithms and Performance Assessment," *Florida Sol. Energy Cent. FSEC-PF-270-95,* pp. 1–88, 1995.

[29]   D. Robinson and A. Stone, "Irradiation modelling made simple: the cumulative sky approach and its applications," in *Proc. PLEA Conference, Eindhoven, Netherlands*, 2004, pp. 19–22.

[30]   I. Photon Engineering, "FRED Optimum software." 2015.

[31]   R. Perez, R. Seals, and J. Michalsky, "All-weather model for sky luminance distribution—preliminary configuration and validation," *Sol. energy*, vol. 50, no. 3, pp. 235–245, 1993.

[32]   R. Siegel and J. Howell, *Thermal Radiation Heat Transfer*. .

[33]   I. M. Slauch, M. G. Deceglie, T. J. Silverman, and V. E. Ferry, "Spectrally Selective Mirrors with Combined Optical and Thermal Benefit for Photovoltaic Module Thermal Management," *ACS Photonics*, vol. 5, no. 4, pp. 1528–1538, 2018.